Limits of turbulence and outer scale profiling with non-Kolmogorov statistics

Jonatan Lehtonen[a], Carlos M. Correia[b], and Tapio Helin[c]

[a,c]University of Helsinki, Finland
[b]Aix Marseille Univ, CNRS, CNES, LAM, Marseille, France

ABSTRACT

SLODAR (SLOpe Detection And Ranging) methods recover the atmospheric turbulence profile from cross-correlations of wavefront sensor (WFS) measurements, based on known turbulence models. Our work grows out of several experiments showing that turbulence statistics can deviate significantly from the classical Kolmogorov/von Kármán models, especially close to the ground. We present a novel SLODAR-type method which simultaneously recovers both the turbulence profile in the atmosphere and the turbulence statistics at the ground layer – namely the slope of the spatial frequency power law. We consider its application to outer scale (L_0)-reconstruction and investigate the limits of the joint estimation of such parameters.

Keywords: SLODAR, turbulence, adaptive optics, tomography, non-Kolmogorov turbulence, outer scale

1. INTRODUCTION

Astronomical Adaptive Optics (AO) systems refer to technology deployed on ground-based optical telescopes, improving imaging quality by providing real-time compensation of disruptive optical aberrations caused by atmospheric turbulence.[1] They are poised to become mainstream in the next generation instruments and telescopes.

After the successful application on single-conjugated AO systems, current and soon-to-be desings attempt to provide correction over larger fields of fiew, typically on the order of tens of arcseconds to a few arcminutes.[2] The latter rely on the tomographic estimation (and subsequent correction) of the turbulence above the telescope, which is an ill-posed problem.[2,3] To this aim, several measurements along different lines-of-sight are used before optimizing the optical correction by driving deformable mirrors with optimal opposite shapes.[4] On account of the small angles (around 1–7 arcmin) and limited computational resources, any successful solution strategy in atmospheric tomography is based on reliable statistical modeling of the turbulence and effective discretization of the atmosphere, i.e. prior knowledge of the *turbulence profile* and the spatial statistics of turbulence.

The goal of this paper is to investigate means to refine the tomographic reconstruction step by providing improved prior information extracted directly from AO telemetry (i.e. actual measurements of the turbulent wavefronts).[5] Here we focus only on methods similar to SLODAR (SLOpe Detection And Ranging[6]), which utilize spatial correlations in the observations of incoming light (wavefront sensor measurements) to recover the turbulence profile. There are two common approaches to this: some authors deduce the profile from wavefront cross-correlations by deconvolution with the autocorrelation of the data,[6,7] while others[5,8–12] formulate a linear dependency between the spatial cross-correlations and the vertical turbulence profile by assuming that the turbulence statistics at any altitude is accurately described by the Kolmogorov or von Kármán model.[13–15] However, deviations from these classical models have been well-documented close to the ground[16–18] and in the upper troposphere and stratosphere.[19–21] Moreover, the turbulence taking place in the telescope dome (so-called *dome seeing*) is well-known to have a spectrum that deviates strongly from the Kolmogorov power law.[10] In consequence, there is a clear need to further develop the current profiling methods to take into account the
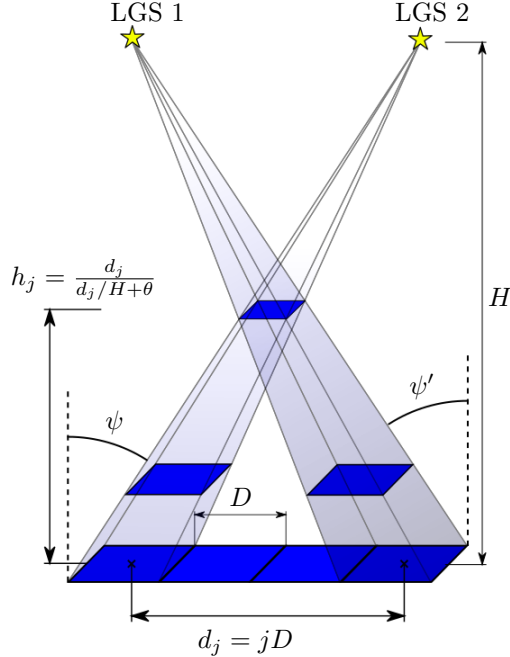
Figure 1. Illustration of the SLODAR measurement setup, showing a row of WFS subapertures measuring wavefronts from two LGSs. The correlation of these measurements is a sum of the wavefront slope correlations between two square-shaped areas in each layer of turbulence. In particular, these areas coincide in the layer at altitude h_j, which depends on subaperture separation d_j, LGS altitude H and LGS separation $\theta = \psi - \psi'$.

uncertainty of the underlying turbulence statistics. A first step towards this can be found in Ref. 22, where the spatial power spectrum at the ground is discretized and estimated along with the turbulence profile.

In this paper we investigate the capability to jointly estimate both the vertical turbulence profile above the ground, and the turbulence spectrum power law and outer scale (L_0) at the ground. These last two parameters can be highly correlated since L_0 creates a knee at low spatial-frequencies which can be interpreted as a change of the overall power law during the minimization fitting procedure. This feature makes an accurate estimation more challenging.

For completeness, we assume that the turbulence is a statistically isotropic and homogeneous random field, which in practice may not be the case for dome seeing. The physics and statistical law of turbulence in the telescope dome is still a matter of research.[23]

We begin by introducing the SLODAR method in Section 2, and modifying it to solve for the ground layer power spectral density (PSD) in Section 3. Sections 4 and 5 describe our numerical simulations of the AO system, including the simulation of boiling phase screens. In Section 6 we motivate solving for the ground layer PSD by showing that it can also significantly improve the turbulence profile itself when the ground layer is non-Kolmogorov. In Section 7 we apply uncertainty quantification methods to explore the limits of outer scale profiling by showing how the stability of SLODAR-based L_0-profiling deteriorates for outer scales larger than the telescope diameter. Finally, the results and future prospects are discussed in Section 8.

2. BACKGROUND TO SLODAR-BASED METHODS

Our work is based on a SLODAR-type method which recovers the vertical turbulence profile by establishing a linear dependence between the profile and correlations of wavefront sensor (WFS) measurements.[5] In this section, we will briefly outline this "standard" SLODAR method, which we then modify in Section 3 to solve for the ground layer power spectral density (PSD). For a more detailed description, we refer the interested readers to Ref. 22.

We consider a pair of laser guide stars* (LGS) at $H = 90\,\text{km}$ with angular coordinates $(\psi, 0)$ and $(\psi', 0)$, as shown in Fig. 1. Following the work of Gilles and Ellerbroek,[5] we deal with the tip/tilt and focus insensitivity of LGS WFSs by instead considering the local curvature:

$$m_\alpha(\boldsymbol{x}_p) = s_\alpha(\boldsymbol{x}_p - D\boldsymbol{e}_\alpha) - 2s_\alpha(\boldsymbol{x}_p) + s_\alpha(\boldsymbol{x}_p + D\boldsymbol{e}_\alpha), \tag{1}$$

where $\alpha = x$ or $\alpha = y$, $s_\alpha(\boldsymbol{x}_p)$ is the wavefront slope in direction α for a subaperture located at $\boldsymbol{x}_p$, $\boldsymbol{e}_\alpha = (1, 0)$ when $\alpha = x$ and $\boldsymbol{e}_\alpha = (0, 1)$ when $\alpha = y$, and D is the subaperture size.

We assume for simplicity that the guide stars are aligned with subaperture rows of the wavefront sensor. The correlation of measurements m_α from two subapertures separated by a distance $\boldsymbol{d}_j = (d_j, 0)$ can then be related to the turbulence strength ρ_l at altitudes h_l through

$$\text{Cor}^\alpha(\boldsymbol{d}_j) = \sum_{l=0}^{L} \frac{1}{D^4} \left(\int_{\mathbb{R}^2} e^{-2\pi i \boldsymbol{\xi} \cdot (\eta_l \boldsymbol{d}_j - h_l \boldsymbol{\theta})} \Psi_0(\boldsymbol{\xi}) |g_l^\alpha(\boldsymbol{\xi})|^2 d\boldsymbol{\xi} \right) \rho_l, \tag{2}$$

where $\boldsymbol{\xi}$ is the spatial frequency vector, $\boldsymbol{\theta} = (\psi - \psi', 0)$ is the LGS separation, $\eta_l = 1 - h_l/H$ is the LGS cone compression factor, and $g_l^\alpha(\boldsymbol{\xi}) = 8\pi i \eta_l \xi_\alpha D^2 \sin^2(\pi \eta_l D \xi_\alpha) \,\text{sinc}(\eta_l D \xi_x) \,\text{sinc}(\eta_l D \xi_y)$ is a weighting function derived in Ref. 22. The correlations $\text{Cor}^\alpha(\boldsymbol{d}_j)$ are thus weighted Fourier transforms of the PSD $\Psi_0(\boldsymbol{\xi})$, which is given by the von Kármán model as

$$\Psi_0(\boldsymbol{\xi}) = 0.0229 \left(|\boldsymbol{\xi}|^2 + L_0^{-2} \right)^{-11/6}. \tag{3}$$

Above, L_0 is the so-called *outer scale* of turbulence, which creates a cut-off at low spatial frequencies to give the spectrum finite variance. The exponent $-11/6$ will be referred to as the Kolmogorov or von Kármán exponent, to distinguish it from the more general power laws we will consider in later sections.

On the other hand, the correlations can be empirically estimated from the measurements m_α through

$$\text{Cor}^\alpha(\boldsymbol{d}_j) \approx \frac{1}{N_j^\alpha} \sum_{i=1}^{N_j^\alpha} \langle m_\alpha(\boldsymbol{x}_i) m'_\alpha(\boldsymbol{x}_i + \boldsymbol{d}_j) \rangle, \tag{4}$$

where m_α and m'_α are measurements from the two WFSs according to (1), $\langle \cdot \rangle$ denotes a time series average, and the sum is taken over all valid subaperture pairs†, with N_j^α denoting the number of such pairs for a given separation $\boldsymbol{d}_j$. Collecting the integrals in (2) into matrices $\boldsymbol{A}^x$ and $\boldsymbol{A}^y$, we obtain the matrix equation

$$\boldsymbol{A}\boldsymbol{\rho} = \begin{pmatrix} \boldsymbol{A}^x \\ \boldsymbol{A}^y \end{pmatrix} \boldsymbol{\rho} = \begin{pmatrix} \boldsymbol{b}^x \\ \boldsymbol{b}^y \end{pmatrix} = \boldsymbol{b}, \tag{5}$$

where $\boldsymbol{\rho}$ is the vertical turbulence profile, and $b_j^\alpha = \text{Cor}^\alpha(\boldsymbol{d}_j)$ as given by (4). The turbulence profile $\boldsymbol{\rho}$ can then be found as the solution to the least-squares problem

$$\min_{\boldsymbol{\rho} \geq \boldsymbol{0}} \| \boldsymbol{A}\boldsymbol{\rho} - \boldsymbol{b} \|_{\boldsymbol{\Sigma}}^2, \tag{6}$$

where $\| \boldsymbol{x} \|_{\boldsymbol{\Sigma}}^2 = \boldsymbol{x}^T \boldsymbol{\Sigma}^{-1} \boldsymbol{x}$, and $\boldsymbol{\Sigma}$ is the covariance matrix for the noise in measurement vector $\boldsymbol{b}$; this can for example be a diagonal matrix where the diagonal entries are inversely proportional to the number of valid subaperture pairs for each element of $\boldsymbol{b}$. It is important to note that the primary source of noise in $\boldsymbol{b}$ is not WFS measurement noise, but rather the fact that the measurements in (4) are estimated as an average of a finite time series of WFS data from a randomly fluctuating atmosphere.

---

*The method is of course applicable also to natural guide stars, with minor modifications: the cone compression factor is neglected, and WFS measurements are used directly, as the local curvature trick in (1) is only necessary for LGSs.

†The subaperture pair is called valid if both $\boldsymbol{x}_i$ and $\boldsymbol{x}_i + \boldsymbol{d}_j$ correspond to illuminated WFS subapertures. For LGSs, a further requirement is that the neighboring subapertures are illuminated, so that m_α can be computed according to (1).

3. MODIFIED SLODAR-METHOD

We now modify the standard SLODAR matrix equation (5) by treating the ground layer PSD as an unknown. This is accomplished by discretizing the PSD and the turbulence strength at the ground through

$$\rho_0 \Psi(\boldsymbol{\xi}) = \sum_{k=0}^{K} \psi_k f_k(|\boldsymbol{\xi}|), \tag{7}$$

where ψ_k are non-negative coefficients and $f_k(\xi)$ are non-negative basis functions satisfying $f_k(\xi_k) = 1$ for given discretization points $0 = \xi_0 < \xi_1 < \cdots < \xi_K$ and $\sum_{k=0}^{K} f_k(\xi) = 1$ for all $0 \leq \xi \leq \xi_K$. Substituting (7) into (2) yields

$$\mathrm{Cor}^{\alpha}(\boldsymbol{d}_j) = \sum_{k=0}^{K} \frac{1}{D^4} \left(\int_{\mathbb{R}^2} e^{-2\pi i \boldsymbol{\xi} \cdot (\eta_0 \boldsymbol{d}_j - h_0 \boldsymbol{\theta})} f_k(|\boldsymbol{\xi}|) |g_0^{\alpha}(\boldsymbol{\xi})|^2 d\boldsymbol{\xi} \right) \psi_k + \sum_{l=1}^{L} A_{jl}^{\alpha} \rho_l, \tag{8}$$

where A_{jl}^{α} are elements of $\boldsymbol{A}^{\alpha}$. Collecting the integrals above into new matrices $\boldsymbol{B}^x$ and $\boldsymbol{B}^y$ and combining them into a single matrix $\boldsymbol{B}$ as we did before, we finally obtain

$$\boldsymbol{A}\boldsymbol{\rho} + \boldsymbol{B}\boldsymbol{\psi} = \boldsymbol{b}, \tag{9}$$

where $\boldsymbol{\psi}$ contains the coefficients ψ_k from (7). Note carefully that the first element of $\boldsymbol{\rho}$ and the first column of $\boldsymbol{A}$ have been removed, as the ground layer is now expressed by the term $\boldsymbol{B}\boldsymbol{\psi}$.

In Ref. 22, we present several methods for solving (9), but in this work we focus on the simplest approach by assuming that the unknown PSD is a power law. Thus, we define the coefficients ψ_k in (7) as

$$\psi_k(c, \gamma, L_0) = c(\xi_k^2 + L_0^{-2})^{-\gamma}, \tag{10}$$

where ξ_k is the discretization point corresponding to the coefficient ψ_k. This reduces the number of unknowns in the PSD to only three: the coefficient c, exponent γ and outer scale L_0. However, the discretization still serves an important purpose by significantly reducing the computational cost, as we can use the matrix equation in (9) instead of having to evaluate the expensive integrals in (8).

Using the form given in (10) for $\boldsymbol{\psi}$, we can then solve the nonlinear least-squares problem

$$\min_{\boldsymbol{\rho}, c, \gamma, L_0 \geq 0} \|\boldsymbol{A}\boldsymbol{\rho} + \boldsymbol{B}\boldsymbol{\psi}(c, \gamma, L_0) - \boldsymbol{b}\|_{\boldsymbol{\Sigma}}^2, \tag{11}$$

where $\|\boldsymbol{x}\|_{\boldsymbol{\Sigma}}^2$ and $\boldsymbol{\Sigma}$ are defined as in (6). From a Bayesian point-of-view, if we impose a uniform prior with a non-negativity constraint, then (11) is equivalent to maximizing the posterior probability distribution of the unknown parameters conditioned on the measurement $\boldsymbol{b}$:

$$p(\boldsymbol{\rho}, c, \gamma, L_0 | \boldsymbol{b}) \sim \exp\left(-\tfrac{1}{2} \|\boldsymbol{A}\boldsymbol{\rho} + \boldsymbol{B}\boldsymbol{\psi}(c, \gamma, L_0) - \boldsymbol{b}\|_{\boldsymbol{\Sigma}}^2 \right), \qquad \boldsymbol{\rho}, c, \gamma, L_0 \geq 0. \tag{12}$$

In addition to this, we will assume that L_0 is at most $200 \, \mathrm{m}$, as this is well beyond what can be sensed with a $40 \, \mathrm{m}$-class telescope.

We solve the minimization problem in (11) with `fmincon`, the Matlab function for constrained nonlinear multivariate minimization, using the `'sqp'`-algorithm with default options except for an optimality tolerance of 10^{-10} and a limit of 30000 iterations. The measurement vector $\boldsymbol{b}$ was normalized to avoid numerical problems. Solving (11) in this way takes only a few seconds on a laptop; typically the time-consuming part of SLODAR is computing the correlations from (4), but even this can be done in real time.

4. SIMULATION DETAILS

The simulations were done using MOST, a MATLAB tool for simulating adaptive optics systems, developed by the AAO team at JKU Linz in Austria. We simulated an AO system with the following properties:

- 37 m telescope with two WFSs, each having 74×74 subapertures ($D = 0.5$ m); the corresponding LGSs were at an altitude of $H = 90$ km, separated by $\boldsymbol{\theta} = (7.5', 0')$

- the WFS photon noise level corresponded to a flux of 50 photons per subaperture per frame[‡]

- 61-layer atmosphere simulated as discrete layers of von Kármán turbulence, with $r_0 = 20$ cm and $L_0 = 25$ m

- layer altitudes were the same as used by SLODAR, corresponding to subaperture pairs with separation $d_j = jD$, where j ranges from 0 to 60; as shown in Fig. 1, these altitudes are $h_j = \frac{d_j}{d_j/H + \theta}$, giving a maximum altitude of 12 km with an average resolution of 200 m

- 52 % of the turbulence strength was located at the ground layer, which was modelled as von Kármán-like turbulence with both the outer scale and exponent as free parameters:

$$\Psi_{\text{ground}} = 0.0229(|\boldsymbol{\xi}|^2 + L_0^{-2})^{-\gamma} \tag{13}$$

Measurements were taken from 1800 independent realizations of this atmosphere, which was found to correspond to five minutes of data from phase screens with simulated boiling. Section 5 below gives a detailed explanation of how this was determined.

5. BOILING PHASE SCREENS

Our goal was to simulate data that realistically corresponds to a measurement time of five minutes. However, AO systems are typically simulated according to Taylor's frozen flow hypothesis,[24] which is not valid over such large timespans; indeed, it may only be valid on time scales of a few hundred milliseconds.[10, 25] This is particularly a problem because it can take several seconds for wind to carry the phase screen over a 37 m telescope, which means that the phase screens decorrelate too slowly. A more suitable model including turbulence dynamics such as boiling is therefore required to ensure realistic noise levels in the SLODAR data.

Motivated by the above, we simulated boiling phase screens using an auto-regressive method.[26] This is done by replacing a given percentage of each phase screen with a new realization having the same power spectral density, which causes the phase screens to change slowly while keeping the same statistics. In Ref. 26, the authors estimated boiling rates using on-sky data from the Gemini Planet Imager, and found boiling coefficients of 0.991 to 0.996 for a 1000 Hz system; this number indicates how much of the original phase screen is carried forward by frozen flow, with the rest being replaced by a new phase screen due to boiling. As consecutive time steps are very strongly correlated, the computational load can be reduced by settling for a 100 Hz system, for which the equivalent boiling coefficients are $0.991^{10} \approx 0.914$ and $0.996^{10} \approx 0.961$. In the end we chose the value 0.95, which means that 5 % of the phase screen changes with each 10 ms time step.

However, the computational cost of simulating even a 100 Hz system for five minutes with boiling is significant, as it corresponds to generating 30000 atmospheres with 61 layers each. Consecutive timesteps are still strongly correlated, but increasing the time step duration further would degrade the measurements, since using every WFS measurement gives more information about the turbulence than using for example every tenth measurement. In an effort to further reduce the computational load, we used statistical analysis to find the number of fully uncorrelated samples of the atmosphere that corresponds to five minutes of boiling data. To this end, we simulated a single layer of turbulence at the ground for one minute with a boiling coefficient of 0.95 at 100 Hz, with a wind speed of $10 \, \text{m s}^{-1}$. As SLODAR data is an average of a correlated time series, we used a method described in Ref. 27 to estimate its variance, i.e. the noise level of the SLODAR data. Given this information, it is easy to find how many independent realizations of the atmosphere give the same variance.

[‡]The photon flux may seem weak for an LGS, but we have found that the noise from this actually has little impact on our results since the noise in the SLODAR data still comes primarily from random fluctuations of the atmosphere.
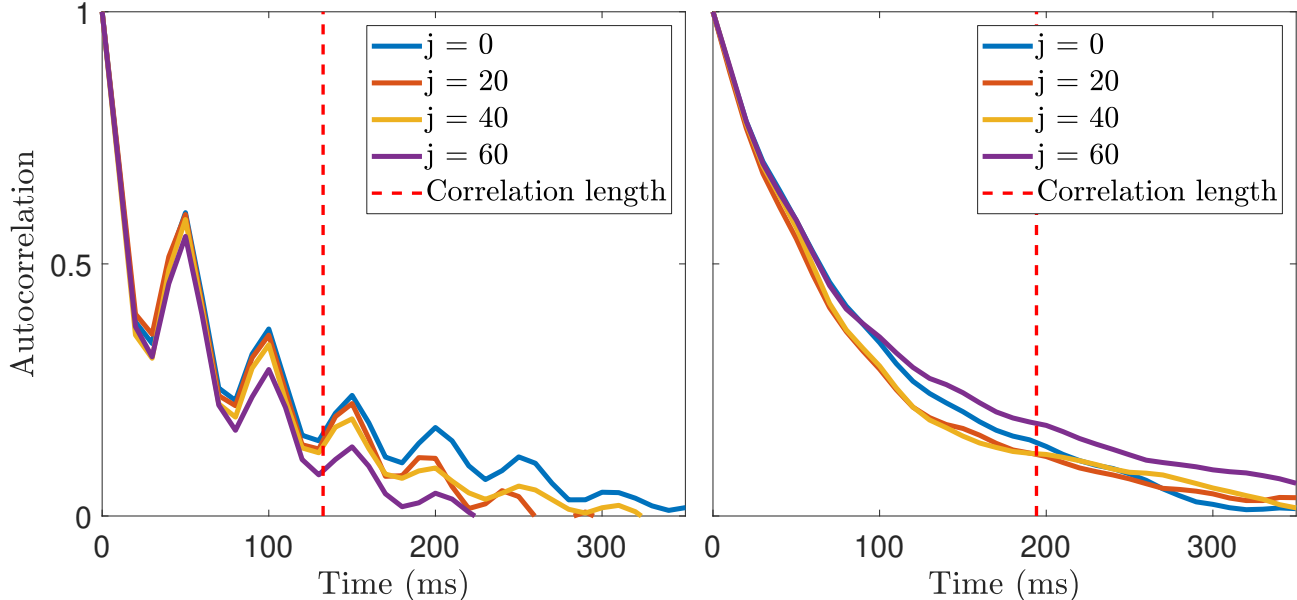
Figure 2. Autocorrelation sequences of one minute of boiling data for subaperture pairs separated by j subapertures, with $j = 0, 20, 40, 60$. Results for x- and y-slopes are shown on the left and right, respectively, and the correlation lengths are indicated by dashed vertical lines. The oscillation in the left image is due to wind being along the x-axis; the peaks occur every $50\,\mathrm{ms}$, since the wind speed is $10\,\mathrm{m\,s^{-1}}$ and the subaperture size is $0.5\,\mathrm{m}$.

Following the method in Ref. 27, we used autocorrelation sequences of time series from boiling data to find its correlation length, which is the amount of data that corresponds to a single uncorrelated realization of the atmosphere. In Fig. 2, we have plotted the autocorrelation sequences for a minute of boiling data for subaperture pairs separated by 0, 20, 40 and 60 subapertures. The images show results for x- and y-directional slope measurements, respectively. The oscillations in the image on the left are due to the wind speed being along the x-axis. Correlation lengths were estimated separately for each element of the measurement vector $\boldsymbol{b}$, i.e. for subaperture separations jD where j ranges from 0 to 60. The mean correlation lengths for x- and y-slopes were $133\,\mathrm{ms}$ and $194\,\mathrm{ms}$, respectively. Their average is $164\,\mathrm{ms}$, which gives us approximately 1800 uncorrelated atmosphere realizations in five minutes, as mentioned in Section 4.

6. IMPACT OF PSD ON PROFILING ACCURACY

One of the main motivations for our method is to provide better prior information about turbulence at the ground. Moreover, in this section we demonstrate that solving the ground layer PSD can also significantly improve overall profiling accuracy. To this end, we have simulated the setup described in Section 4 for five different PSD exponents at the ground: -1.55, -1.65, -1.75, -1.95, and the usual $-11/6 \approx -1.833$. All of these ground layer PSDs were simulated for a wide range of outer scale values. In order to reduce the computational load and the fluctuation between different data sets, we used the same 60-layer atmosphere realizations for turbulence above the ground, only changing the simulated ground layer phase screen for each data set.

We compare different turbulence profiles by defining a relative C_n^2-profile error on all layers except the ground[§], given by

$$E_{C_n^2}(\boldsymbol{\rho}) = \frac{\sum_{l=1}^{L} |\rho_l - \rho_l^{\mathrm{true}}|}{\sum_{l=1}^{L} \rho_l^{\mathrm{true}}}, \tag{14}$$

where ρ_l^{true} is the simulated turbulence strength on the lth layer. Of course, there is no direct connection between this error metric and e.g. tomographic error. The goal is not to predict how the error in the profile will affect

---

[§]The ground layer is excluded as comparing values of C_n^2 for PSDs with different exponents is quite non-trivial.
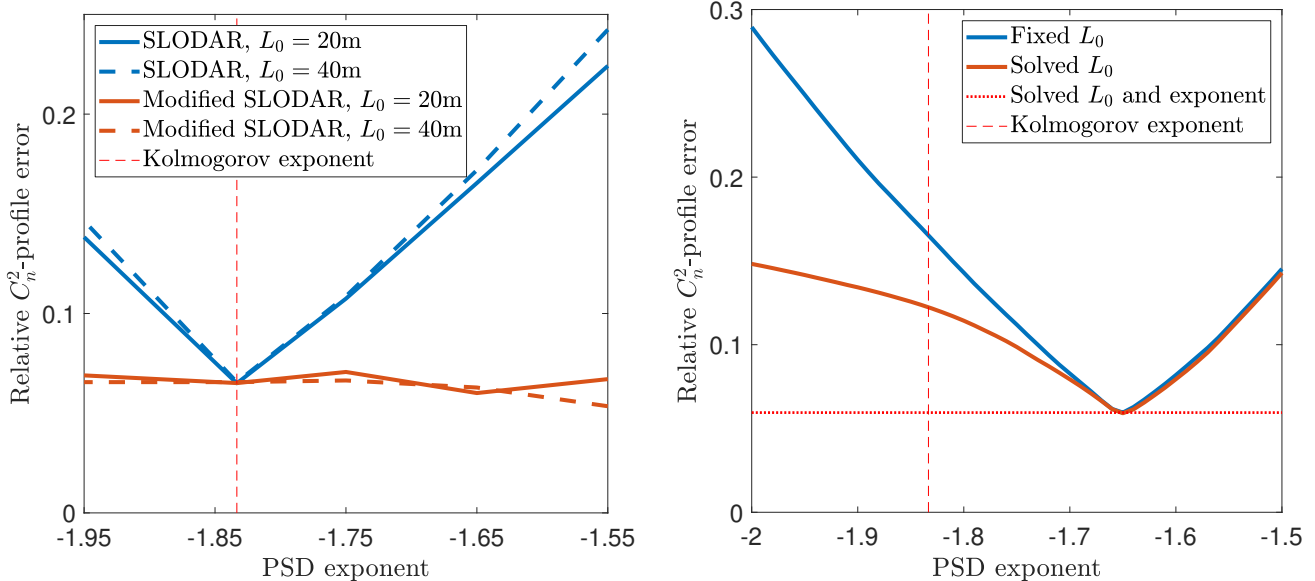
Figure 3. These plots show the relative C_n^2-profile error caused by assuming the wrong exponent for the ground layer PSD. On the left, our method and standard SLODAR have been applied to data sets with exponents of -1.55, -1.65, -1.75, $-11/6$ and -1.95, with outer scales of $20\,\mathrm{m}$ and $40\,\mathrm{m}$. On the right, a single data set with $L_0 = 20\,\mathrm{m}$ and an exponent of -1.65 is used. The blue and red curve indicate the profile errors given by fixing the exponent to the value indicated on the horizontal axis, and either fixing $L_0 = 20\,\mathrm{m}$ (blue) or solving for L_0 as well (red). The dotted red line indicates the error level obtained by solving for both L_0 and the exponent. In both figures, the dashed red line is the Kolmogorov exponent.

performance in systems using that profile, but rather to highlight that assuming the wrong turbulence statistics for the ground layer may cause systematic errors in the profile reconstruction.

Fig. 3 shows the error $E_{C_n^2}$ in two different cases. On the left, both standard SLODAR and our variation of it have been applied to data sets with each of the five PSD exponents listed above, for outer scales of $20\,\mathrm{m}$ and $40\,\mathrm{m}$; for standard SLODAR, the true outer scales for all 61 layers were used, to ensure that any bias is strictly due to the PSD exponent. As can be seen, the profile error for our method is almost independent of the PSD exponent, while standard SLODAR yields increasingly worse results as the exponent deviates more from the assumed Kolmogorov exponent of $-11/6$.

The plot on the right in Fig. 3 shows results for a single data set with $L_0 = 20\,\mathrm{m}$ and an exponent of -1.65, where our method was applied with various parameters fixed. The blue curve corresponds to fixing $L_0 = 20\,\mathrm{m}$; for the red curve, this was treated as an unknown. In both cases, the PSD exponent was fixed to the value indicated on the horizontal axis. Thus, the relative error for standard SLODAR can be found at the intersection of the blue curve and the dashed line indicating the Kolmogorov exponent. The error level obtained when both L_0 and the exponent are solved from the SLODAR data is indicated by the dotted line; this error comes from the noisy reconstructions at higher altitudes, which is primarily due to the limited measurement time and the low number of subaperture pairs available for large separations.

An important point related to the second image in Fig. 3 is that while solving L_0 does reduce the relative C_n^2-profile error, this comes at the cost of reconstructing a non-physical value for L_0 at the ground. For example, using the Kolmogorov exponent of $-11/6$ gives an outer scale of $5.37\,\mathrm{m}$ for the ground, and even being off by 0.05 gives $12.0\,\mathrm{m}$ and $56.9\,\mathrm{m}$ for the exponents -1.7 and -1.6, respectively. This highlights the need for joint estimation of the exponent and L_0, and also explains why the error is reduced very little for exponents larger than -1.65: with a larger exponent the method tries to compensate by using a larger value of L_0, but this has very little impact on the turbulence profile since SLODAR data is quite insensitive to large outer scales.

Fig. 4 shows an example of the turbulence profiles corresponding to the second image in Fig. 3. The profiles have been split into two images, with the first three layers above the ground layer in the first plot and the
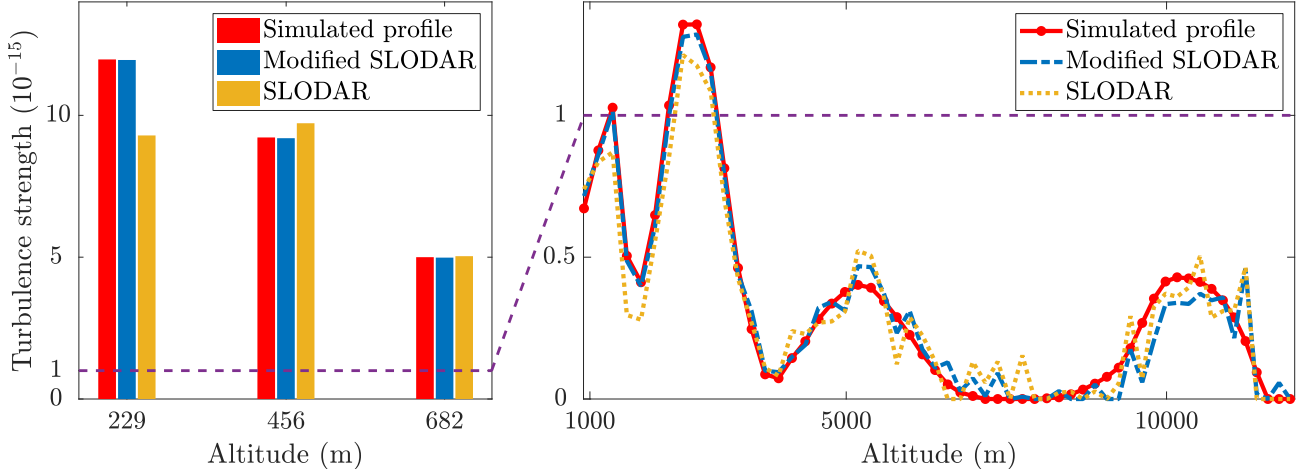
Figure 4. An example of two turbulence profile reconstructions corresponding to the errors shown in the second image of Fig. 3, where the true exponent is -1.65 and $L_0 = 20\,\mathrm{m}$. The simulated profile is shown in red, the reconstruction using our method in blue, and the one from standard SLODAR (using the true L_0) in orange; the values given by our method were -1.6531 for the exponent and 19.9285 for L_0. The ground layer is omitted as the profiles use different PSDs for it, which means there is no clear way to compare the profiles at the ground layer. The next three layers above the ground layer are shown separately since their magnitude is much bigger than that of the other layers; this is indicated by the dashed purple line which shows where the value 10^{-15} lies in both plots. As can be seen, using the Kolmogorov exponent led to significant errors in the first layer and the layers between $1\,\mathrm{km}$ and $3\,\mathrm{km}$.

remaining layers in the second, since the first three have significantly higher magnitude than the rest; this is also indicated by the dashed purple line, which is at the same turbulence strength of 10^{-15} in both images. As these profiles correspond to Fig. 3, the true exponent for the ground layer was -1.65 and the outer scale was $20\,\mathrm{m}$. The true profile is shown in red, the reconstruction with our method in blue, and the one using standard SLODAR in orange; note that for SLODAR, the true outer scale of $20\,\mathrm{m}$ was used at the ground, rather than assuming an outer scale of $25\,\mathrm{m}$ for the whole atmosphere.

It is clear from Fig. 4 that a majority of the error seen in Fig. 3 comes from misestimating the second layer, although the reconstruction with standard SLODAR also underestimates the turbulence between $1\,\mathrm{km}$ and $3\,\mathrm{km}$. The benefit from estimating the ground layer PSD is clear, as the reconstruction is almost perfect up to roughly $5\,\mathrm{km}$ in altitude. After that the noise in the measurements begins to dominate, as there are fewer subaperture pairs available with separations long enough to properly measure turbulence at the higher altitudes. Beyond $3\,\mathrm{km}$ there is no significant difference in reconstruction quality between the two profiles, as misestimating the ground layer appears to primarily impact the reconstruction quality of layers close to it.

7. QUANTIFYING L_0-UNCERTAINTY

How reliably can we expect to recover L_0 from SLODAR data? This is an important question for outer scale profiling. Our goal is to provide an upper limit on the level of accuracy that can be expected, as simulations are in many ways an idealization of the real world. We investigate this by using an adaptive Markov chain Monte Carlo (MCMC) method[28] to sample the posterior probability distribution of the unknown parameters $\boldsymbol{\rho}, c, \gamma$ and L_0. This distribution is given by (12), with some additional constraints on the parameters as described in Section 3. This distribution essentially gives the probability that a given set of parameter values produced the measurement vector $\boldsymbol{b}$, which means we can use it for uncertainty quantification to find e.g. the variance and marginal distribution of each parameter.

We consider data sets with standard von Kármán turbulence for all layers; only the outer scale value for the ground is varied. Using the Delayed Rejection Adaptive Metropolis -method (DRAM) described in Ref. 28, we generated chains of 3500000 samples to accurately probe the posterior probability distribution given by
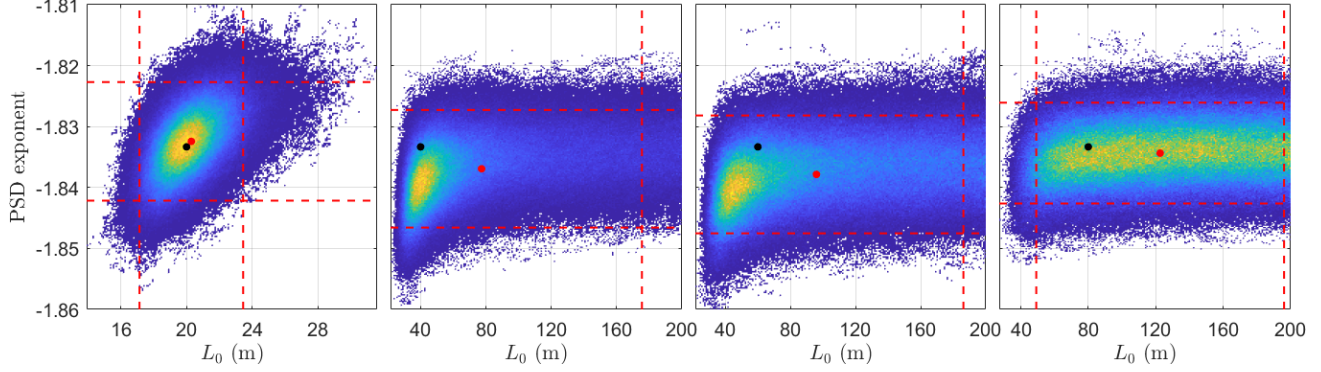
Figure 5. Marginal distribution of L_0 and the PSD exponent; the simulated values of L_0 are 20 m, 40 m, 60 m and 80 m, from left to right. The y-axis scale is the same in each image. The black dot is the true value for L_0 and the exponent, and the red dot is the mean of the probability distribution, also known as the conditional mean (CM) estimate. The dashed lines represent 95 % credible intervals around the CM estimate, i.e. 95 % of the distribution lies between the two parallel lines. Note that the horizontal axis is scaled very differently in the first image.
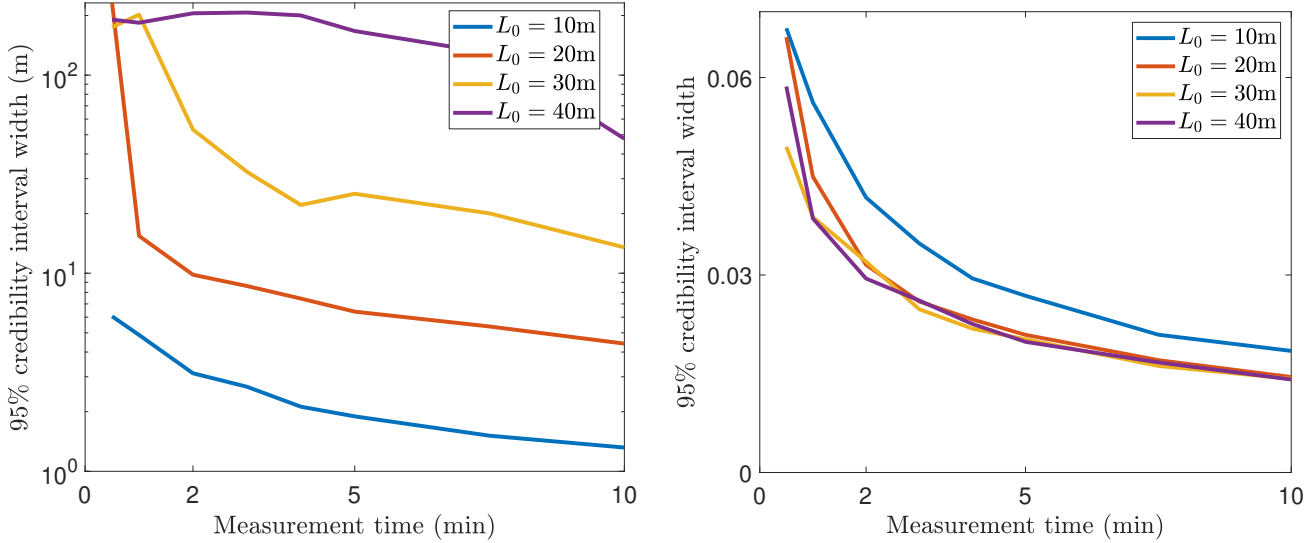

Figure 6. The width of the 95 % credibility intervals for the posterior distributions as a function of measurement time, with L_0 shown on the left and the exponent on the right. These credibility intervals were obtained from data sets with von Kármán turbulence at the ground, for four different values of L_0. Several data sets with a varying number of samples were used; the time shown on the horizontal axis is based on the baseline of 1800 independent atmosphere realizations per five minutes.

(12). Fig. 5 shows the marginal distribution of L_0 and the PSD exponent as two-dimensional histograms of the MCMC chains, for $L_0 = 20$ m, 40 m, 60 m and 80 m. Note carefully that the horizontal axis is scaled differently for $L_0 = 20$ m, as there is far less uncertainty about the value of L_0 in this case.

Fig. 5 shows that the uncertainty in reconstructing L_0 grows rapidly as the true value of L_0 increases, which is also shown by the CM estimate being so far from the true values in all but the first image; this is due to a significant part of the probability distribution being located at higher values of L_0. However, the maximum of the posterior distribution is actually quite close to the true values when $L_0 = 40$ m, and this is also the solution that we use, as described at the end of Section 3. Unfortunately, even the maximum is quite far off when $L_0 = 60$ m, and in the case of $L_0 = 80$ m there does not even appear to be a unique maximum.

An important thing to keep in mind is that the uncertainty in the parameters depends on the amount of measurements we have; the results shown in this section and Section 6 are for five minutes of data. However, Fig. 6 shows how this uncertainty depends on measurement time, with up to ten minutes of data for L_0 ranging

from 10 m to 40 m; the plots show the credibility interval for L_0 and the exponent, respectively. As we would expect, the credibility interval becomes smaller as we have more data; in fact, both the L_0 and exponent credibility interval widths seem to exhibit an asymptotic $t^{-1/2}$-decay, which is precisely the decay for the standard deviation of noise in SLODAR data. In principle resolving larger values of L_0 is then only a matter of having enough data, although this may require very long measurement times. In practice, however, the atmospheric parameters evolve in time, which limits how much data we can actually use.

An interesting point in Fig. 6 is that there is actually more uncertainty about the exponent when $L_0 = 10$ m. This may seem counter-intuitive, but there is a good reason for this: as L_0 gets smaller, the exponent becomes more sensitive to small changes in L_0, and so uncertainty in L_0 translates to uncertainty in the exponent. This can also be seen in Fig. 5 as a downward trend in the distributions. When L_0 is 80 m, its value makes almost no difference for the exponent, but a clear correlation is visible in the case where L_0 is 20 m. In a way, the non-linearity of solving L_0 and the exponent becomes worse as L_0 becomes smaller; in the worst case, when L_0 is much smaller than a single subaperture, it becomes impossible to distinguish between the outer scale and the exponent, as the PSD is almost flat in the spatial frequency range which is visible to SLODAR.

8. DISCUSSION

We have presented a SLODAR-type method for simultaneously solving both the turbulence profile and the ground layer PSD, and applied it to simulated data from 1800 independent realizations of the atmosphere, which we have found corresponds to five minutes of data with simulated boiling phase screens. Using this data, we have demonstrated the benefits of solving the ground layer PSD by using a relative C_n^2-profile error as a metric, and further we have applied uncertainty quantification techniques to determine the feasibility of reconstructing L_0 with SLODAR-based methods.

We have found that allowing a more general model for the ground layer PSD in the presence of non-Kolmogorov turbulence can provide significantly more accurate profiling than assuming von Kármán turbulence, while maintaining the same level of accuracy in cases where the turbulence is von Kármán. We also found that L_0-profiling can in some cases mitigate the model errors to a limited extent, but this comes at the cost of strong biases in the recovered values of L_0, exemplified by the fact that changing the PSD exponent by only 0.05 in either direction gave values of 12 m and 57 m for L_0 when the true value was 20 m. This seems to indicate that modeling non-Kolmogorov turbulence is necessary to recover accurate L_0-profiles, as the outer scale is very sensitive to even small changes in the PSD exponent.

We have also found that the uncertainty in outer scale profiling grows quite rapidly as a function of L_0, to the point where recovering outer scales just 50 % larger than the telescope diameter can already be very unstable. Moreover, the sensitivity to the PSD exponent becomes stronger as the value of L_0 increases. However, it should be mentioned that these results were obtained by simulating LGSs; in principle, natural guide stars would give slightly better results for L_0-profiling, as the removal of tip/tilt and focus from the data due to LGSs reduces the sensitivity to L_0.

An important thing to note is that we used a flat prior for L_0, meaning that all values between 0 m and 200 m were considered equally likely prior to the measurements. Good prior information from a reliable source could help improve the L_0-reconstruction by imposing a more informative prior distribution on L_0. This could for example help eliminate the heavy tails in the posterior distributions shown in Fig. 5. We have also found that accurate modeling of the system can be extremely vital for something as unstable as outer scale profiling, since even slight modeling errors can cause significant errors in L_0.

ACKNOWLEDGMENTS

REFERENCES

[1] Tyson, R. K., [*Principles of Adaptive Optics*], CRC press (2015).

[2] Ellerbroek, B. L. and Vogel, C. R., "Inverse problems in astronomical adaptive optics," *Inverse Prob.* **25**(6), 063001 (2009).

[3] Ramlau, R., Saxenhuber, D., and Yudytskiy, M., "Iterative reconstruction methods in atmospheric tomography: FEWHA, Kaczmarz and Gradient-based algorithm," in [*SPIE Astronomical Telescopes+ Instrumentation*], *Proc. SPIE* **9148**, 9148 – 9148 – 15 (2014).

[4] Roddier, F., [*Adaptive Optics in Astronomy*], Cambridge University Press (1999).

[5] Gilles, L. and Ellerbroek, B. L., "Real-time turbulence profiling with a pair of laser guide star Shack–Hartmann wavefront sensors for wide-field adaptive optics systems on large to extremely large telescopes," *J. Opt. Soc. Am. A* **27**(11), A76–A83 (2010).

[6] Wilson, R. W., "SLODAR: measuring optical turbulence altitude with a Shack-Hartmann wavefront sensor," *MNRAS* **337**(1), 103–108 (2002).

[7] Wang, L., Schöck, M., and Chanan, G., "Atmospheric turbulence profiling with SLODAR using multiple adaptive optics wavefront sensors," *Appl. Opt.* **47**(11), 1880–1892 (2008).

[8] Guesalaga, A., Neichel, B., Correia, C., Butterley, T., Osborn, J., Masciadri, E., Fusco, T., and Sauvage, J.-F., "Online estimation of the wavefront outer scale profile from adaptive optics telemetry," *MNRAS* **465**(2), 1984–1994 (2017).

[9] Cortés, A., Neichel, B., Guesalaga, A., Osborn, J., Rigaut, F., and Guzman, D., "Atmospheric turbulence profiling using multiple laser star wavefront sensors," *MNRAS* **427**(3), 2089–2099 (2012).

[10] Guesalaga, A., Neichel, B., Cortés, A., Béchet, C., and Guzmán, D., "Using the C_n^2 and wind profiler method with wide-field laser-guide-stars adaptive optics to quantify the frozen-flow decay," *MNRAS* **440**(3), 1925–1933 (2014).

[11] Butterley, T., Wilson, R. W., and Sarazin, M., "Determination of the profile of atmospheric optical turbulence strength from SLODAR data," *MNRAS* **369**(2), 835–845 (2006).

[12] Védrenne, N., Michau, V., Robert, C., and Conan, J.-M., "C_n^2 profile measurement from Shack–Hartmann data," *Opt. Lett.* **32**(18), 2659–2661 (2007).

[13] Panchev, S., [*Random Functions and Turbulence: International Series of Monographs in Natural Philosophy*], vol. 32, Elsevier (2016).

[14] Kolmogorov, A. N., "The local structure of turbulence in incompressible viscous fluid for very large Reynolds numbers," *Dokl. Akad. Nauk SSSR* **30**(4), 301–305 (1941).

[15] Kolmogorov, A. N., "A refinement of previous hypotheses concerning the local structure of turbulence in a viscous incompressible fluid at high Reynolds number," *J. Fluid Mech.* **13**(01), 82–85 (1962).

[16] Buser, R. G., "Interferometric determination of the distance dependence of the phase structure function for near-ground horizontal propagation at 6328 Å," *J. Opt. Soc. Am.* **61**(4), 488–491 (1971).

[17] Dayton, D., Pierson, B., Spielbusch, B., and Gonglewski, J., "Atmospheric structure function measurements with a Shack–Hartmann wave-front sensor," *Opt. Lett.* **17**(24), 1737 (1992).

[18] Bester, M., Danchi, W. C., Degiacomi, C. G., Greenhill, L. J., and Townes, C. H., "Atmospheric fluctuations: empirical structure functions and projected performance of future instruments," *Astrophys. J.* **392**, 357–374 (1992).

[19] Kyrazis, D. T., Wissler, J. B., Keating, D. D. B., Preble, A. J., and Bishop, K. P., "Measurement of optical turbulence in the upper troposphere and lower stratosphere," in [*Laser Beam Propagation and Control*], *Proc. SPIE* **2120**, 2120 – 2120 – 13 (1994).

[20] Belen'kii, M. S., Karis, S. J., Osmon, C. L., Brown II, J. M., and Fugate, R. Q., "Experimental evidence of the effects of non-Kolmogorov turbulence and anisotropy of turbulence," in [*ICO XVIII 18th Congress of the International Commission for Optics*], *Proc. SPIE* **3749**, 3749 – 3749 – 2 (1999).

[21] Bruce E. Stribling, Byron M. Welsh, M. C. R., "Optical propagation in non-Kolmogorov atmospheric turbulence," *Proc. SPIE* **2471**, 2471 – 2471 – 16 (1995).

[22] Helin, T., Kindermann, S., Lehtonen, J., and Ramlau, R., "Atmospheric turbulence profiling with unknown power spectral density," *Inverse Prob.* **34**(4), 044002 (2018).

[23] Lombardi, G., Melnick, J., Goñi, R. H., Navarrete, J., Sarazin, M., Berdja, A., Tokovinin, A., Wilson, R., Osborn, J., Butterley, T., and Shepherd, H., "Surface layer characterization at Paranal Observatory," in [*SPIE Astronomical Telescopes+ Instrumentation*], *Proc. SPIE* **7733**, 7733 – 7733 – 13 (2010).

[24] Taylor, G. I., "The spectrum of turbulence," *Proc. R. Soc. Lond. A* , 476–490 (1938).

[25] Ono, Y. H., Correia, C. M., Andersen, D. R., Lardire, O., Oya, S., Akiyama, M., Jackson, K., and Bradley, C., "Statistics of turbulence parameters at Maunakea using the multiple wavefront sensor data of RAVEN," *MNRAS* **465**(4), 4931–4941 (2017).

[26] Srinath, S., Poyneer, L. A., Rudy, A. R., and Ammons, S. M., "Computationally efficient autoregressive method for generating phase screens with frozen flow and turbulence in optical simulations," *Opt. Express* **23**(26), 33335–33349 (2015).

[27] Flyvbjerg, H. and Petersen, H. G., "Error estimates on averages of correlated data," *J. Chem. Phys.* **91**(1), 461–466 (1989).

[28] Haario, H., Laine, M., Mira, A., and Saksman, E., "DRAM: efficient adaptive MCMC," *Stat. Comput.* **16**(4), 339–354 (2006).